



Magnetic Field of the Eclipsing M-dwarf Binary YY Gem

Oleg Kochukhov¹ and Denis Shulyak²

¹ Department of Physics and Astronomy, Uppsala University, Box 516, SE-75120 Uppsala, Sweden; oleg.kochukhov@physics.uu.se

² Max-Planck Institute for Solar System Research, Justus-von-Liebig-Weg 3, D-37077 Göttingen, Germany

Received 2018 November 21; revised 2019 February 11; accepted 2019 February 11; published 2019 March 6

Abstract

YY Gem is a short-period eclipsing binary system containing two nearly identical, rapidly rotating, very active early M dwarfs. This binary represents an important benchmark system for calibrating empirical relations between fundamental properties of low-mass stars and for testing theories of interior structure and evolution of these objects. Both components of YY Gem exhibit inflated radii, which has been attributed to poorly understood magnetic activity effects. Despite a long history of magnetic activity studies of this system, no direct magnetic field measurements have been made for it. Here we present a comprehensive characterization of the surface magnetic field in both components of YY Gem. We reconstructed the global field topologies with the help of a tomographic inversion technique applied to high-resolution spectropolarimetric data. This analysis revealed moderately complex global fields with a typical strength of 200–300 G and anti-aligned dipolar components. A complementary Zeeman intensification analysis of the disentangled intensity spectra showed that the total mean field strength reaches 3.2–3.4 kG in both components of YY Gem. We used these results together with other recent magnetic field measurements of M dwarfs to investigate the relation between the global and small-scale fields in these stars. We also assessed predictions of competing magnetoconvection interior structure models developed for YY Gem, finding that only one of them anticipated the surface field strength compatible with our observations. Results of our starspot mapping of YY Gem do not support the alternative family of theoretical stellar models, which attempts to explain the radius inflation by postulating a large spot filling factor.

Key words: binaries: eclipsing – stars: activity – stars: fundamental parameters – stars: individual (YY Gem) – stars: magnetic field

Supporting material: machine-readable table

1. Introduction

Detached eclipsing binary systems provide a unique possibility of a model-independent determination of fundamental parameters of their stellar components (Torres et al. 2010). In particular, a combined analysis of the photometric observations of eclipses and radial velocity variation of individual components enables one to infer stellar radii and masses with a precision of a few percent. This, in turn, permits comprehensive tests of predictions of the stellar evolution and model atmosphere theories.

A striking result emerging from recent analyses of low-mass eclipsing binary systems is the finding that standard stellar evolutionary models underestimate the observed stellar radii by 5%–15% (e.g., Torres & Ribas 2002; Ribas 2006; Morales et al. 2009a, 2009b). Many of the systems exhibiting this discrepancy are short-period binaries with rapidly rotating components. Such late-type stars are expected to host stronger magnetic fields as a result of enhanced efficiency of the rotationally powered dynamo (Marsden et al. 2014; Vidotto et al. 2014). Therefore, it was proposed that magnetic activity associated with a rapid stellar rotation might be responsible for the observed radius inflation of late-type close binary stars (Chabrier et al. 2007; López-Morales 2007; Morales et al. 2008).

Two types of effects are considered as plausible mechanisms of the interplay between magnetic field and stellar radii. On the one hand, formation of dark cool spots in the magnetized areas at the stellar surface suppresses radiative losses resulting in a radius increase compared to unspotted stars of the same luminosity (Chabrier et al. 2007; Morales et al. 2010; Jackson & Jeffries 2014).

On the other hand, inflated radii can be explained by the modification of stellar structure by the magnetic suppression or stabilization of the interior convection (Mullan & MacDonald 2001; Feiden & Chaboyer 2012, 2013, 2014; MacDonald & Mullan 2013, 2014, 2017b). The relative importance of these two effects as a function of stellar mass and the validity of alternative theoretical approaches to treating magnetoconvection in one-dimensional stellar structure models are hotly debated topics. Detailed observations and comprehensive modeling of selected benchmark binary systems are necessary to inform this debate and guide further theoretical development.

YY Geminorum (Castor C, HD 60179 C, BD +32°1582, GJ 278 C) is a key object for understanding the impact of magnetic activity on the fundamental properties of low-mass stars. This is a close, double-line, eclipsing binary system with an orbital period of 0.81 days containing two nearly identical active dM1e stars. YY Gem is a part of the remarkable sextuplet system α Gem (Castor). Both Castor A and B are young, early-type spectroscopic binaries. The association with the α Gem group provides additional stringent constraints on the age and metallicity of YY Gem. The physical parameters of the YY Gem components were studied in detail by Torres & Ribas (2002). These authors determined the mean stellar radius ($0.6191 R_{\odot}$) and mass ($0.5992 M_{\odot}$) with an accuracy of better than 1% and demonstrated that these radii exceed theoretical predictions by 10%–20%. YY Gem is one of only four M-dwarf eclipsing binaries with properties measured accurately enough to enable meaningful tests of stellar evolutionary models (Torres 2013). It is thus extensively used as a reference object for empirical mass and radius calibrations (e.g., Torres et al. 2010; Eker et al. 2015; Moya et al. 2018). A number of theoretical studies attempted to explain

the inflated radii of the components of YY Gem by developing different versions of nonconventional stellar interior structure models that incorporated effects of magnetic field and surface inhomogeneities (Feiden & Chaboyer 2013; Jackson & Jeffries 2014; MacDonald & Mullan 2014, 2017b).

The ubiquitous manifestations of the magnetic activity of YY Gem, including frequent flaring, broadband photometric and emission-line variability, and nonthermal X-ray and ultraviolet emission, have been investigated by many authors. Since the seminal work by Kron (1952), the out-of-eclipse photometric variation of YY Gem was interpreted in the context of the rotational modulation caused by a patchy, nonuniform surface brightness distribution on one or both components (Torres & Ribas 2002; Butler et al. 2015). Large and frequent flare events have been reported for the system and investigated with the help of multiwavelength monitoring campaigns spanning the frequency range from X-ray to radio (Butler et al. 2015, and references therein). YY Gem was also targeted by several comprehensive X-ray imaging and spectroscopic studies (Güdel et al. 2001; Stelzer et al. 2002; Hussain et al. 2012), which demonstrated that both components are extremely active and flaring frequently. Detailed magnetohydrodynamical models of flares have been developed using YY Gem as a test bed (Gao et al. 2008).

Many previous studies emphasize the central role of the magnetic field and related surface inhomogeneities for interpretation of the multitude of activity phenomena in the YY Gem system and for explaining anomalous radii of its binary components. However, literature contains little direct, quantitative information on the magnetic field properties and surface structure morphology of YY Gem A and B. Several studies attempted to model the out-of-eclipse photometric time series observations of the combined light from the system in terms of dark surface spots (Torres & Ribas 2002; Butler et al. 2015). Such analyses generally require strong assumptions regarding the spot characteristics (e.g., spot shapes and spot-to-photosphere contrast have to be prescribed) and often struggle to constrain spot latitudes or unambiguously assign them to one or another component. A spectroscopic surface mapping with the help of the Doppler imaging (DI) method is potentially capable of providing more reliable and higher-resolution information on the surface spot distributions, although it has its own caveats when applied to equator-on stars such as the components of YY Gem. Preliminary DI maps of both components of YY Gem were presented by Hatzes (1995), but this work was not followed up with a detailed study. No direct measurements of the mean magnetic field modulus are available for YY Gem. The global magnetic field geometry of the components has not been characterized in detail either.

The main aim of our investigation of YY Gem is to supply observational constraints to magnetoconvection interior structure models of low-mass stars by performing a comprehensive characterization of the surface magnetic field of both components. This requires a detailed spectroscopic and spectropolarimetric analysis of the system. As a by-product, this analysis yields revised estimates of the fundamental parameters of the components and enables us to study their inhomogeneous surface brightness distributions. The rest of this paper is organized as follows. Section 2 describes observational material used in our study. The procedure of deriving the mean intensity and polarization profiles is presented in Section 3. Section 4 discusses binary spectral

disentangling and presents a revised spectroscopic orbit of YY Gem. Section 5 briefly describes the methodology of Doppler and Zeeman–Doppler imaging (ZDI) of double-line binary systems and presents results of application of this tomographic mapping technique to YY Gem A and B. Finally, the summary of our main findings and discussion of their implications are given in Section 7.

2. Observational Data

Our investigation of YY Gem is based on a set of archival high-resolution spectropolarimetric observations obtained with the ESPaDOnS spectropolarimeter at the Canada–France–Hawaii Telescope (CFHT). This instrument provides simultaneous coverage of the 370–1050 nm wavelength interval at the resolving power of $R = 65,000$ and allows one to record either linear or circular polarization spectra in addition to the usual intensity observations. YY Gem was observed in the circular polarization mode, in the period from 2012 January 4 to 17. With typically three observations per night, this campaign resulted in 36 individual circular polarization observations. Each of these observations consisted of four 420 s subexposures, between which the polarimeter was reconfigured to exchange the optical path and detector positions of the orthogonal polarization beams. As discussed by Bagnulo et al. (2009), this spatiotemporal polarimetric modulation technique is highly effective in removing spurious and instrumental polarization features. The ESPaDOnS spectra were reduced by the UPENA pipeline running the LIBRE-ESPRIT software (Donati et al. 1997).

We have used the CFHT Science Archive³ interface to retrieve 36 Stokes V observations and 144 Stokes I spectra corresponding to individual polarimetric subexposures. These data were reprocessed by improving continuum normalization with the method described by Rosén et al. (2018). In addition, we calculated Heliocentric Julian Dates (HJDs) of midexposures from the time stamps provided in the ESPaDOnS data files using Astrolib⁴ IDL routines.

According to the diagnostic information available from the headers of the pipeline-reduced ESPaDOnS spectra, the median signal-to-noise ratio (S/N) of the Stokes I spectra of YY Gem is 280 per extracted spectrum pixel at $\lambda = 870$ nm. The random photon noise of the circular polarization spectra is characterized by the median S/N of 510 relative to the continuum of the corresponding Stokes I spectra. Columns (1) and (3) of Table 1 report individual HJD and S/N values, respectively, for all 144 Stokes I spectra analyzed here. The set of 36 Stokes V observations discussed in our paper corresponds to groups of four consecutive entries in Table 1.

It should be noted that while the 420 s exposure time of individual subexposures is negligible compared to the 0.81-day orbital period of YY Gem, the total time (≈ 1805 s) of acquiring four such subexposures composing a single Stokes V observation corresponds to 2.6% of the orbital cycle. The radial velocities of the YY Gem components can change by up to ≈ 25 km s⁻¹ during this time interval. It is therefore essential to account for the resulting orbital radial velocity smearing in any analysis of the Stokes V data.

³ <http://www.cadc-ccda.hia-ihp.nrc-cnrc.gc.ca/en/cfht>

⁴ <https://idlastro.gsfc.nasa.gov>

Table 1
Radial Velocity Measurements of the YY Gem Components

Reduced HJD	Phase	S/N	V_A (km s^{-1})	V_B (km s^{-1})	Orb. Fit
55,930.8055	0.723	309	122.31	-116.84	y
55,930.8109	0.729	313	123.10	-117.77	y
55,930.8162	0.736	305	123.67	-118.23	y
55,930.8215	0.743	306	124.05	-118.59	y
55,930.9408	0.889	297	79.95	-76.95	y
55,930.9462	0.896	289	76.07	-73.05	y
55,930.9515	0.902	286	72.03	-68.99	y
55,930.9569	0.909	282	68.30	-64.19	y

(This table is available in its entirety in machine-readable form.)

3. Least-squares Deconvolved Profiles

Similar to most other cool active stars, circular polarization signatures are too weak to be detected in individual spectral lines of YY Gem. In this situation a multiline polarization diagnostic technique is required to derive high-quality average Stokes V profiles suitable for reliable magnetic field detection and detailed modeling of the global surface field topology. Calculation of the mean intensity profiles also provides input spectra for precise radial velocity measurements of binary star components.

In this study we employed the least-squares deconvolution (LSD; Donati et al. 1997) technique in its implementation by Kochukhov et al. (2010). This multiline method approximates stellar spectra as a superposition of spectral lines represented by a scaled and shifted mean profile. Using this representation, equivalent to convolution of a mean profile and a line mask in the velocity space, one can compute mean intensity or polarization spectra with a series of matrix operations. The input data necessary for this calculation consist of an observed spectrum, corresponding error bars, and a line mask containing information on the line positions and relative weights (line depth for Stokes I and the product of line depth, wavelength, and the effective Landé factor for Stokes V).

We used the VALD3 database⁵ (Ryabchikova et al. 2015) together with the solar metallicity MARCS (Gustafsson et al. 2008) model atmosphere with $T_{\text{eff}} = 3800$ K and $\log g = 4.5$ (Torres & Ribas 2002) to compile an absorption line list appropriate for the YY Gem components. The final LSD line mask, comprising 5059 atomic lines, was derived by excluding spectral regions affected by broad stellar features or telluric absorption and then selecting lines with the residual depth greater than 0.2 of the continuum. The polarization line weights were normalized according to the mean wavelength $\lambda_0 = 636$ nm and the mean effective Landé factor $z_0 = 1.22$.

The LSD line-averaging procedure was applied separately to the 144 Stokes I spectra corresponding to individual polarimetric subexposures and to the Stokes I and V spectra comprising 36 complete circular polarization observations. Representative Stokes I and V LSD profiles are illustrated in Figure 1 for two orbital phases. This figure also shows the Stokes I LSD spectra corresponding to groups of four consecutive spectropolarimetric subexposures. It is evident that these spectra exhibit non-negligible radial velocity shifts due to the orbital motion of the YY Gem components. It is also

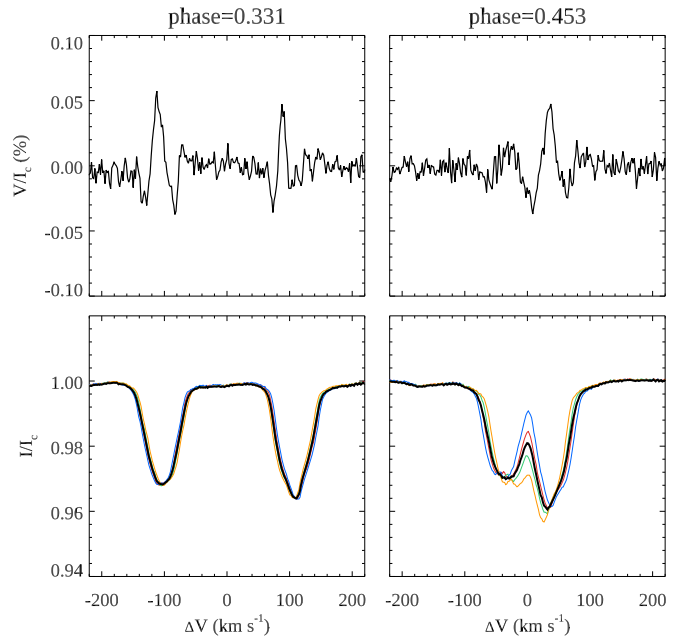


Figure 1. Representative Stokes V (top row) and Stokes I (bottom row) LSD profiles of YY Gem. The two columns show spectra for orbital phase 0.331 (left) and 0.453 (right). The thin colored lines in the bottom panels illustrate the Stokes I profiles corresponding to four spectropolarimetric subexposures.

apparent that the equivalent width of the primary LSD profile (shifted to negative velocities in Figure 1) is systematically smaller compared to the profile of YY Gem B.

Thanks to co-adding information from thousands of individual lines, the Stokes V LSD spectra of YY Gem boast a S/N of $\approx 15,000$ per 1.8 km s^{-1} velocity bin, which corresponds to a factor of 30 gain relative to the polarimetric sensitivity of the original polarization spectra. Variable polarization signatures with a typical semiamplitude of 5×10^{-4} are detected for 34 out of 36 observations with a typical significance (full amplitude of the signal divided by the error bar) of 12σ . The two Stokes V spectra yielding no detection have a greatly inferior quality (S/N of only about 1300 in the LSD Stokes V profiles) compared to the rest of the data and are excluded from subsequent analysis.

4. Spectral Disentangling and Orbital Solution

The spectroscopic binary nature of YY Gem significantly complicates analysis of individual components, due to complex, time-dependent line blending seen in the observed spectra. Nevertheless, redundant information contained in the observations collected at different orbital phases can be exploited to derive accurate radial velocities of the components, obtain their high-quality separated spectra, and study line profile variability. To this end, we applied different spectral disentangling methods to LSD profiles and to selected regions of Stokes I spectra.

First, 144 Stokes I LSD spectra were analyzed with the disentangling code described by Folsom et al. (2010) and applied by several other studies (e.g., Kochukhov et al. 2018; Rosén et al. 2018). This procedure performs an iterative derivation of the binary component velocities and mean profile shapes using a weighted least-squares fit of a set of observed LSD profiles. The method assumes that observations at each orbital phase can be represented by a superposition of two

⁵ <http://vald.astro.uu.se>

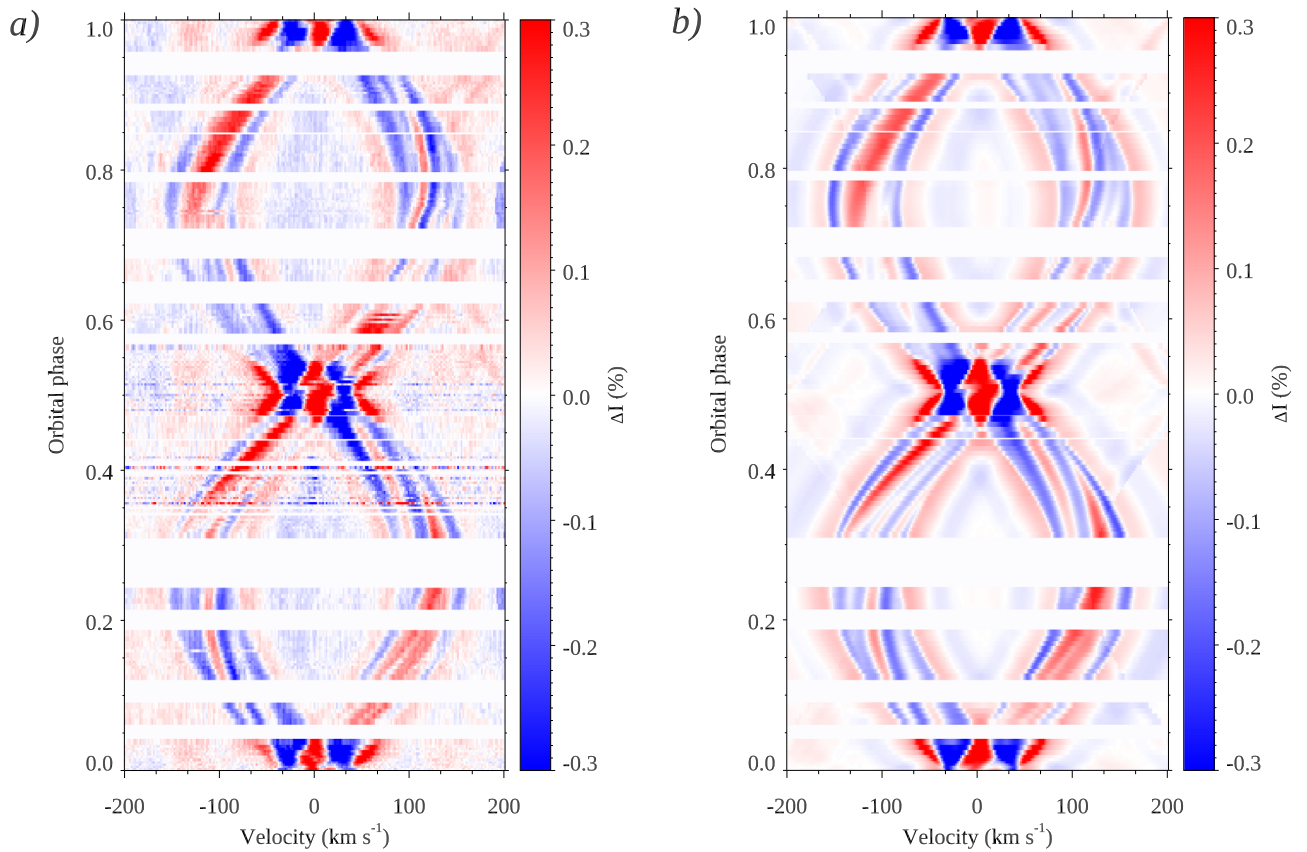


Figure 2. Dynamic residual Stokes I LSD profiles of YY Gem. The (a) observed and (b) model residual spectra are plotted as a function of the orbital phase. The color scale corresponds to $\pm 0.3\%$ intensity range.

constant spectra with variable radial velocity shifts. The disentangling calculation starts with an initial guess of radial velocities of the components, for which we adopted the orbital solution by Torres & Ribas (2002). Mean stellar spectra are then derived with a least-squares optimization algorithm by fitting observations at all available orbital phases. In the next step the individual radial velocities are refined with another least-squares fit, keeping the mean spectra fixed. This two-step procedure was repeated, seven times in this case, until the convergence was achieved for all radial velocities and all spectral bins of the disentangled spectra.

The basic assumption of the disentangling procedure that the intrinsic stellar spectra are constant is not fulfilled during the primary and secondary eclipses. Consequently, our radial velocity estimates are less accurate during that part of the orbit. In addition, the LSD Stokes I profiles of both components of YY Gem are affected by surface spots at all orbital phases. Nevertheless, as demonstrated by Rosén et al. (2018), our binary spectral disentangling procedure is robust against such profile distortions.

The LSD profile disentangling is illustrated in Figure 2(a), which shows dynamic residual Stokes I spectra obtained by subtracting the model two-component spectra from the observed profiles. This plot enables us to assess the intrinsic spectral variability of the components of YY Gem. It is clear that both stars show variability outside eclipses. With an amplitude of a few times 10^{-3} , this variability is relatively weak and is not detectable in typical individual spectral lines. The gradually evolving profile distortions seen in Figure 2(a) reveal surface inhomogeneities, which rotate in and out of

view. The profile variability pattern of both components is perfectly phased with the orbital period, implying a synchronous rotation with $P_{\text{rot}}^A = P_{\text{rot}}^B = P_{\text{orb}}$. There is no evidence of the surface structure evolution within the 13-day time span covered by the observations. The spot signatures encompass the entire width of the line profiles, suggesting that the surface structures responsible for this behavior are located preferentially at low latitudes. One should bear in mind, however, that this residual profile analysis is not sensitive to any axisymmetric surface features, such as polar spots.

The radial velocities of YY Gem A and B⁶ obtained with the help of Stokes I LSD profile disentangling are listed in Columns (4) and (5) of Table 1. Using these data, we redetermined the spectroscopic orbital parameters of YY Gem adopting a fixed orbital period of $P_{\text{orb}} = 0.814282212$ days (Torres & Ribas 2002). The orbital parameters were optimized with a nonlinear least-squares fit in IDL using the MPFIT package (Markwardt 2009) and the `helio_rv` Astrolib routine. A total of 48 radial velocity measurements close to phases 0.0 and 0.5 were excluded from the fit, as indicated by entries in the last column of Table 1.

The observed radial velocities of the YY Gem components are compared to the orbital fit in Figure 3. The standard deviation of this fit is 0.46 km s^{-1} for YY Gem A and 0.65 km s^{-1} for YY Gem B, which represents a factor of 5–7 improvement relative to the radial velocity analysis by Torres & Ribas (2002). The revised orbital parameters are reported in

⁶ Following the naming convention of previous publications, we refer to the star eclipsed at phase 0.0 as the “primary” or “component A.”

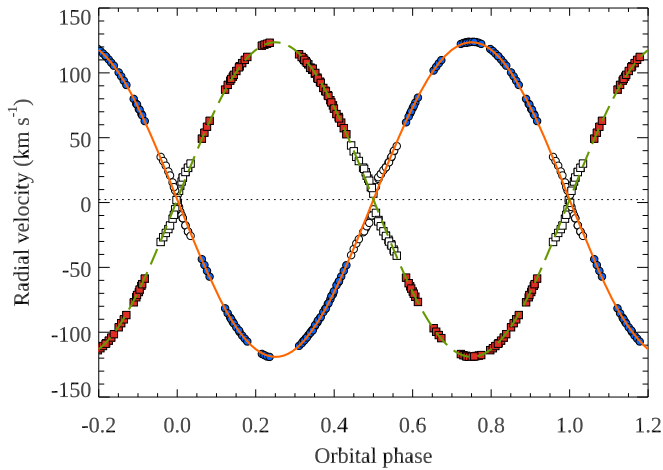


Figure 3. Orbital radial velocity variation of the YY Gem components. The symbols show measurements for the primary (circles) and secondary (squares). The solid and dashed lines illustrate the orbital solution constrained by the radial velocity measurements outside eclipses (filled symbols). Measurements at the eclipse phases (open symbols) are excluded from the fit.

Table 2
Spectroscopic Orbital Solution for YY Gem

Parameter	Value
Fitted quantities:	
P_{orb} (days)	0.814282212^{a}
HJD ₀	$2449345.116643 \pm 0.000068$
K_{A} (km s ⁻¹)	121.337 ± 0.072
K_{B} (km s ⁻¹)	121.264 ± 0.064
γ (km s ⁻¹)	2.287 ± 0.038
e	0.0^{b}
Derived quantities:	
$M_{\text{B}}/M_{\text{A}}$	1.00060 ± 0.00080
$M_{\text{A}} \sin^3 i$ (M_{\odot})	0.60217 ± 0.00058
$M_{\text{B}} \sin^3 i$ (M_{\odot})	0.60253 ± 0.00060
M_{A} (M_{\odot})	$0.60597 \pm 0.00058^{\text{c}}$
M_{B} (M_{\odot})	$0.60633 \pm 0.00061^{\text{c}}$
$a_{\text{A}} \sin i$ ($\times 10^6$ km)	1.35863 ± 0.00081
$a_{\text{B}} \sin i$ ($\times 10^6$ km)	1.35782 ± 0.00072

Notes.

^a Adopted from Torres & Ribas (2002).

^b Circular orbit is assumed.

^c Calculated assuming $i = 86^{\circ}.29 \pm 0^{\circ}.1$ (Torres & Ribas 2002).

Table 2. In agreement with previous studies of YY Gem, we found the orbit to be circular ($e = 0.00035 \pm 0.00028$) and therefore fixed eccentricity to zero in the final orbital fit. The error bars listed in the table are formal uncertainties calculated by MPFIT and result by assigning uncertainties to the RV measurements equal to the standard deviations of the RVs around the best fit quoted above. This procedure results in a reduced chi-square of 1.

Table 2 provides our estimates of the mass ratio $M_{\text{B}}/M_{\text{A}}$, scaled masses $M_{\text{A,B}} \sin^3 i$, and semimajor axes $a_{\text{A,B}} \sin i$. Finally, we report the component masses that follow from our spectroscopic orbital elements and the orbital inclination angle $i = 86^{\circ}.29 \pm 0^{\circ}.1$ (Torres & Ribas 2002). The orbital phases of 144 Stokes I observations calculated with the updated ephemeris are given in the second column of Table 1.

Another version of the spectral disentangling calculation was applied to the 963–985 nm wavelength region in order to obtain

mean component spectra for the magnetic intensification analysis presented below. In this case our goal was to infer the component spectra using previously determined orbital velocities, which simplifies disentangling. On the other hand, the presence of strong, variable telluric absorption in this wavelength region adds a significant complication. Rather than using an observed telluric standard star or theoretical telluric spectrum, we implemented telluric correction as part of the modified spectral disentangling analysis. The observations at each orbital phase were represented with a superposition of the two stellar components plus a telluric contribution. The latter spectrum was assumed to be shifted according to the (known) heliocentric radial velocity correction and scaled for individual observations following the usual power-law relation (e.g., Cotton et al. 2014). This composite spectral model was iteratively fitted to all Stokes I observations simultaneously, yielding telluric-corrected, disentangled time-averaged spectra of YY Gem A and B with an S/N in excess of 500. This three-component disentangling procedure is illustrated in Figure 4, which shows the derived mean stellar spectra, the average telluric spectrum, and the fit to observations for two representative orbital phases.

5. Zeeman–Doppler Imaging

DI and ZDI are powerful inversion techniques for indirect studies of surface structure of cool active stars (Kochukhov 2016). Here we carried out a tomographic reconstruction of the surface brightness and magnetic field maps of both components of YY Gem using the INVERSLSDB binary ZDI code described by Rosén et al. (2018). This indirect imaging method, developed from the INVERSLSD code (Kochukhov et al. 2014), enables mapping of inhomogeneities on the surfaces of one or both components of a spectroscopic binary system using LSD profile intensity and/or polarization observations. The forward spectral modeling implemented in INVERSLSDB accounts for eclipses and can be performed either assuming spherical stellar shapes, an arbitrary eccentric binary orbit, and arbitrary inclinations and rotation periods of the components (typical of wide misaligned binaries) or using the Roche lobe geometry to describe detached or contact corotating binary components with aligned orbital and rotational axes (typical of close binaries). In the present analysis of YY Gem we used the latter Roche lobe geometry mode. This treatment, fully appropriate for this system, implies that the rotation of the components is synchronized with the orbital motion, the stars rotate as solid bodies, and their (generally nonspherical) shapes are given by equipotential surfaces. A set of system parameters necessary for binary spectrum synthesis calculations with INVERSLSDB includes the component masses, the orbital period and inclination, and the two values of Roche surface potentials or, equivalently, stellar polar radii. In addition, one has to specify relative surface brightness of the components to reproduce the observed line depth ratio.

5.1. Brightness Distribution

In the first step of tomographic analysis of YY Gem we modeled the Stokes I LSD profiles with the goal to determine several nuisance parameters and derive stellar brightness distributions. We adopted the orbital parameters and stellar masses according to the results of Section 4. The orbital inclination $i = 86^{\circ}.29$ was taken from Torres & Ribas (2002).

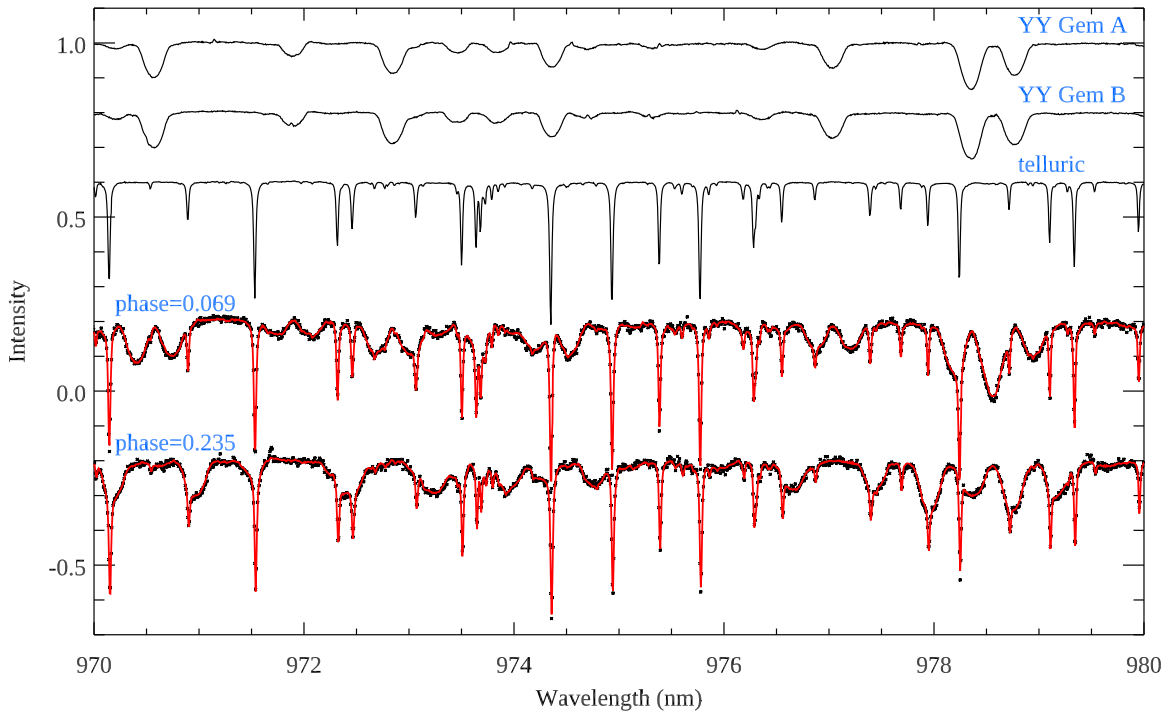


Figure 4. Illustration of the three-component disentangling of YY Gem spectra. The top three curves show the disentangled, time-averaged spectra of YY Gem A and B and the mean telluric absorption spectrum. The bottom curves compare observations (symbols) at two representative orbital phases with the composite model spectra (solid curve) including the stellar and telluric contributions. Spectra are offset vertically for display purposes.

The synthetic LSD profile calculations were based on the Unno–Rachkovsky (Landi Degl’Innocenti & Landolfi 2004) analytical local line profile model. We used the mean line parameters reported in Section 3 and adjusted the local profile width to match the theoretical disk-center LSD profile obtained from the SYNTH3 (Kochukhov 2007) intensity spectrum calculated with the $T_{\text{eff}} = 3800$ K and $\log g = 4.5$ MARCS model atmosphere. Radiative transfer calculations with the same code were used to establish the center-to-limb variation of the continuum intensity at $\lambda = 636$ nm. We found that the square root limb-darkening law (e.g., Claret 2017) with the coefficients $c = 0.115$ and $d = 0.757$ provides the best representation of the model atmosphere predictions.

The equivalent width of the local profile, the relative surface brightness, and the radii of the components were optimized by fitting observations. As a result of this analysis, we established that the best description of the LSD Stokes I profiles of YY Gem is obtained with a surface brightness ratio of $I_A/I_B = 0.88 \pm 0.01$ and equivalent volume radii of $R_A = 0.614 \pm 0.010 R_\odot$ and $R_B = 0.612 \pm 0.010 R_\odot$. The maximum difference between the radii measured along (R_{in}) and perpendicular (R_{pole}) to the axis connecting the centers of masses of the two components is about 1%, implying that YY Gem A and B exhibit a negligible deviation from the spherical shapes.

The unequal surface brightness of the two components introduced above is necessary to reproduce the observed systematically weaker LSD Stokes I profiles of YY Gem A compared to YY Gem B (see Figure 1). This line depth difference can also be reproduced by directly postulating a different equivalent width of the local profiles, leading to the same modeling results. Here we treat I_A/I_B as a nuisance parameter, without attempting to investigate its physical

meaning. Nevertheless, this systematic difference of the line strengths for the two stars with essentially identical mass and radius is somewhat surprising and may indicate a T_{eff} difference of ≈ 90 K.

The final brightness maps derived for the components of YY Gem are presented in the top panels of Figure 5. These continuum brightness distributions were derived using the modified Tikhonov regularization method (see Hackman et al. 2016; Rosén et al. 2018), which numerically stabilizes the surface imaging problem by minimizing the local map contrast and limiting deviation from the default brightness level of the unspotted photosphere. The surface maps in Figure 5 are shown in the Hammer–Aitoff projection. The stellar longitude is counted counterclockwise, in the same direction as the stellar rotation, and increases from left to right in the figure. The central meridian corresponds to the longitude of 180° .

Owing to a large inclination angle, the Doppler mapping method is unable to distinguish the northern and southern stellar hemispheres, except when the surface features are partially obscured during the primary and secondary eclipses. This is why the recovered dark spot geometries are symmetric with respect to the stellar equators everywhere except close to 0° longitude (phase 0.0) for YY Gem A and 180° longitude (phase 0.5) for YY Gem B. The overall continuum brightness contrast required to reproduce observations is relatively small. The darkest feature ($\approx 40\%$ intensity contrast) is found at the surface of YY Gem A very close to the point facing the secondary. YY Gem B shows no corresponding dark spot. Apart from this difference, the components of YY Gem have statistically similar degrees of spot coverage. In agreement with the qualitative Stokes I profile analysis in Section 4, dark spots are found only within the $\pm 30^\circ$ latitude band. Neither star

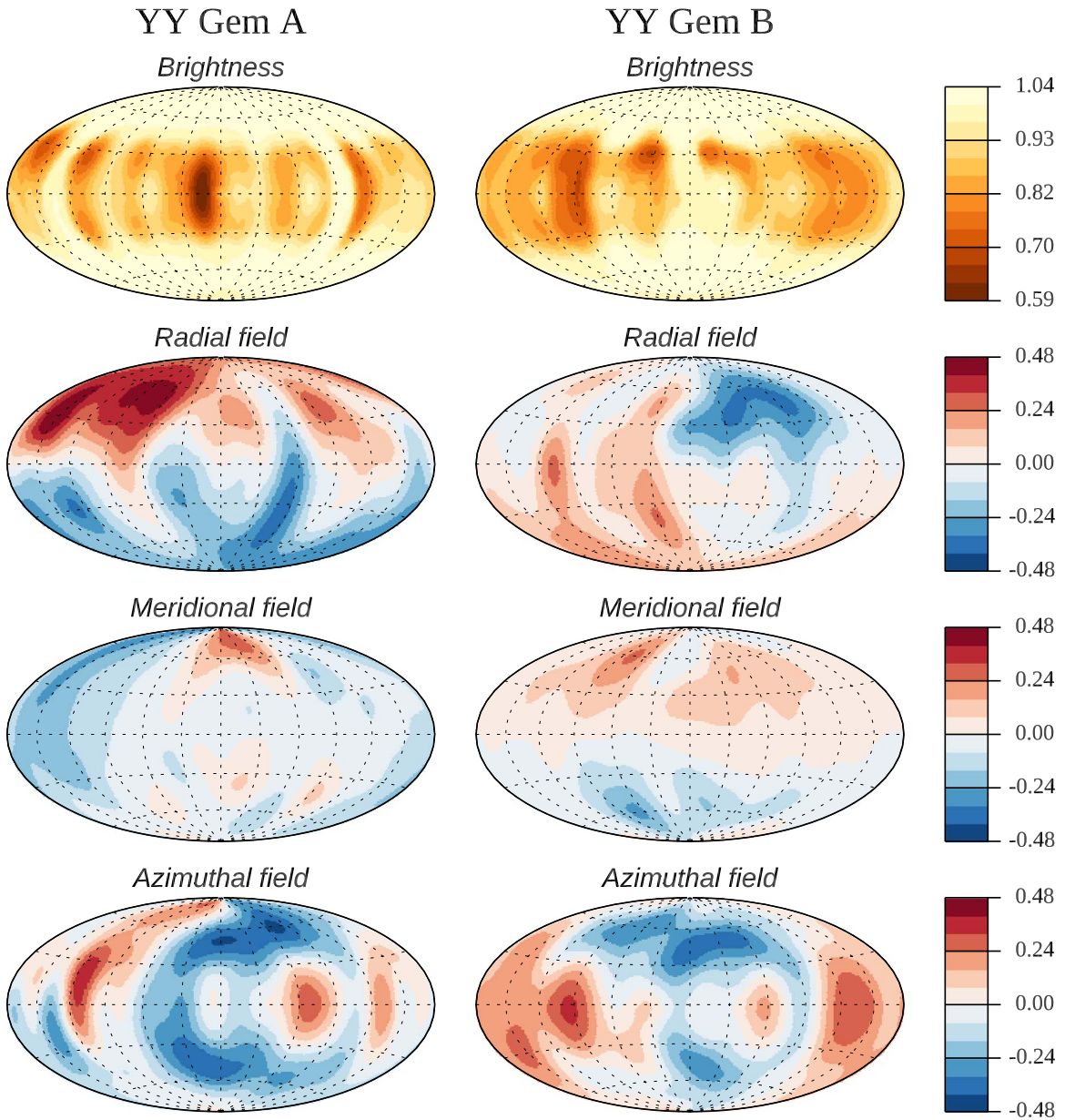


Figure 5. Brightness and magnetic field maps of YY Gem A (left column) and YY Gem B (right column). The surface images are displayed in the Hammer–Aitoff projection, with the central meridian corresponding to 180° longitude. The topmost row shows the brightness distributions obtained from the Stokes I profiles. The second to fourth rows show maps of the radial, meridional, and azimuthal field components derived from the Stokes V spectra. The side color bars indicate the relative continuum brightness and the field strength in kG.

exhibits a polar spot, which agrees with the findings by Hatzes (1995).

Given the large number of observations and a small amplitude of the Stokes I profile variability, it is impractical to document DI analysis with the traditional comparison of the observed and calculated line profiles. Instead, we produced a dynamic residual profile plot similar to Figure 2(a), but using the model LSD profiles as an input for the disentangling procedure. The result is shown in Figure 2(b). The observed residual profile variability pattern is successfully reproduced by the DI binary star model. The out-of-eclipse profile distortions, tracing the brightness inhomogeneities, have the same shape and amplitude as in observations. The largest residuals occur at the eclipse phases and have identical structure in both observations and the model, confirming that these residuals

originate from the intrinsic limitation of the standard spectral disentangling treatment at these orbital phases.

5.2. Global Magnetic Field Topology

We applied ZDI analysis to infer the global magnetic field topologies of the YY Gem components from LSD observations of the circular polarization signatures in metal line profiles. This observable provides detailed information on the geometrical structure of the vector field but is sensitive only to a large-scale, organized magnetic field component. Due to cancellation of polarization signals coming from surface regions with opposite field polarities, small-scale fields do not contribute to the disk-integrated stellar polarization spectra. Therefore, ZDI maps derived here do not inform us about the total magnetic

Table 3
Magnetic Field Characteristics of YY Gem

Parameter	YY Gem A	YY Gem B
From ZDI analysis:		
$\langle B_V \rangle$ (kG)	0.260	0.205
$\langle B_r \rangle$ (kG)	0.168	0.098
$\langle B_h \rangle$ (kG)	0.179	0.162
E_{pol}^a (%)	70.7	71.5
$E_{m < \ell/2}^b$ (%)	58.1	44.8
$E_{\ell=1}^c$ (%)	52.4	45.5
From Zeeman intensification analysis:		
$\langle B_I \rangle$ (kG)	3.44	3.15
B (kG)	4.60	3.65
f	0.75	0.86

Notes.

^a Fractional energy of the poloidal field component.

^b Fractional energy of the axisymmetric field component.

^c Fractional energy of the dipolar field component.

field energy and do not provide a realistic assessment of the total mean field modulus.

With these caveats in mind, we have carried out a tomographic reconstruction of the global field topologies of YY Gem A and B following the ZDI methodology discussed by Kochukhov et al. (2014) for single stars and by Rosén et al. (2018) for binaries. The vector surface field distribution of each star is parametrized in terms of a general spherical harmonic expansion. Three sets of spherical harmonic coefficients are employed to describe the radial poloidal, the horizontal poloidal, and the horizontal toroidal fields. Each set is composed of the spherical harmonic terms with all possible azimuthal numbers m and the angular degrees ℓ from $\ell = 1$ to some maximum value $\ell = \ell_{\text{max}}$. In this study we have chosen $\ell_{\text{max}} = 10$, resulting in 360 spherical harmonic coefficients for each star. All these coefficients are treated as free parameters and are adjusted simultaneously by fitting 34 observed Stokes V LSD profiles, starting from the zero-field initial guess. The inhomogeneous brightness distribution derived in the previous step of Stokes I DI analysis is taken into account in the calculation of synthetic circular polarization spectra.

The line profile synthesis relies on the Unno–Rachkovsky formulae, assuming that the response of the local LSD profile to magnetic field is equivalent to that of a normal Zeeman triplet with the effective Landé factor $z = 1.22$. As mentioned in Section 2, ESPaDOnS polarization observations are constructed from sets of four consecutive subexposures obtained over a non-negligible fraction of the orbital period. We explicitly accounted for the corresponding rotational and orbital phase smearing by calculating each synthetic profile with a five-point trapezoidal integration over an appropriate orbital phase interval.

The magnetic inversion problem is numerically stabilized with the help of the harmonic regularization method (Kochukhov et al. 2014). Specifically, the inversion is constrained by a penalty function, which minimizes the total magnetic field energy of the ZDI map and restricts contributions of higher-order harmonic terms. The optimal regularization parameter is determined following the procedure described by Kochukhov (2017).

The global magnetic field maps of the YY Gem components are shown in Figure 5. Table 3 reports numerical characteristics

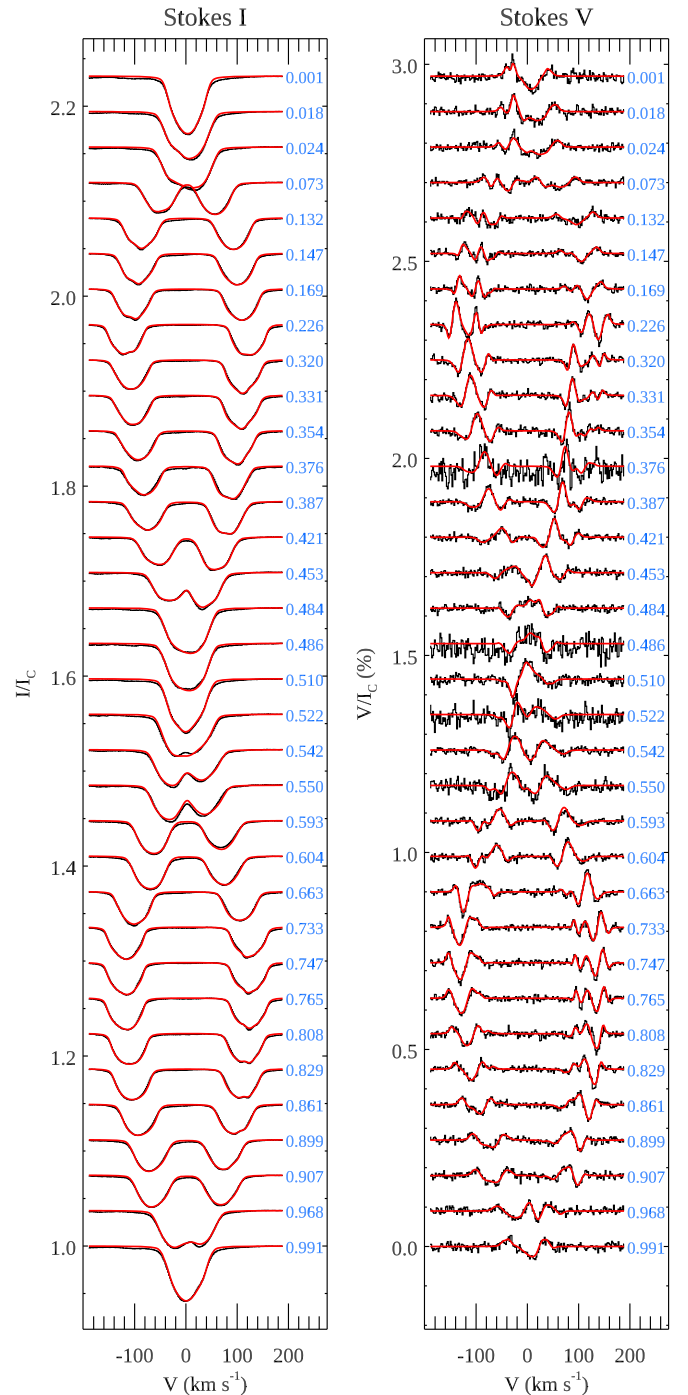


Figure 6. ZDI fit (solid lines) to the observed (histograms) Stokes I and V LSD profiles of YY Gem. The spectra corresponding to different orbital phases are offset vertically. The phases are indicated to the right of each profile.

of these field geometries, which might be of interest in the context of comparison to ZDI results obtained for other active stars. The final Stokes V profile fit provided by the ZDI model is illustrated in Figure 6. The reduced χ^2 of this fit is 0.91, implying that all significant details of the observed polarization signatures are successfully reproduced by the model spectra.

We found that the primary has a somewhat stronger global magnetic field, with the mean field strength of 260 G compared to 205 G for the secondary. The mean unsigned radial magnetic field (e.g., Vidotto et al. 2014) is 168 and 98 G for the primary and secondary, respectively. The maximum surface field

strength is 546 G for YY Gem A and 515 G for YY Gem B. Both stars possess moderately complex global field configurations, dominated by dipolar components (45%–52% of the magnetic field energy is contained in $\ell = 1$ modes), but including $\geq 2\%$ energy contributions for all modes up to $\ell = 7$. The fields of both components of YY Gem are predominantly poloidal (poloidal field contributes 71% of the global field energy) and are split approximately equally between the axisymmetric ($m < \ell/2$) and nonaxisymmetric ($m \geq \ell/2$) harmonic modes. The strictly axisymmetric (the sum of all $m = 0$ modes) part of the magnetic geometries composes 36%–49% of the field energy.

As can be clearly seen from the radial field distributions presented in Figure 5, the dipolar components of the magnetic fields of YY Gem A and B are anti-aligned. The polarity of the field at the stellar north pole is predominantly positive for the primary and negative for the secondary.

We performed a series of 100 bootstrapping magnetic inversions to assess uncertainties of the ZDI results for YY Gem. In each such calculation the residuals of the fit to the LSD Stokes V profiles were randomly reshuffled and added back to the synthetic spectra. The resulting data were subjected to the same tomographic analysis as the original observations. These calculations showed that the local standard deviation of the radial, meridional, and azimuthal magnetic field maps illustrated in Figure 5 is 10–16 G on average. The maximum deviation is 19–27 G. The average magnetic quantities reported in Table 3 are accurate to within 3–6 G. The uncertainty of the fractional energies of different harmonic components is 1.3%–2.8%.

6. Zeeman Intensification Analysis

An analysis of magnetic broadening (for slowly rotating active stars) and intensification (more relevant for fast rotators such as the components of YY Gem) of absorption lines in the intensity spectra provides a powerful magnetic diagnostic method (e.g., Basri et al. 1992; Reiners 2012), which is complementary to, and in some cases more informative than, ZDI mapping of the global field topology. The latter technique can be applied to fields of essentially arbitrary strength and is particularly sensitive to field orientation. However, precisely due to this sensitivity, it yields a grossly underestimated field strength whenever stellar surface is peppered with small regions of opposite field polarity. In contrast, Zeeman broadening and intensification depend almost entirely on the field modulus. This prevents using these effects for inferring detailed surface magnetic field geometries. In addition, the field strength has to exceed ~ 500 G to reliably disentangle magnetic effects from other processes impacting Stokes I spectra. On the other hand, Zeeman intensification provides an unbiased measure of the total magnetic flux density, including both large- and small-scale magnetic fields, and is free of the polarity cancellation problem inherent to most polarimetric diagnostic methods.

Our approach to measuring the total (unsigned) magnetic flux density in the components of YY Gem is based on a direct spectrum synthesis modeling of the Zeeman effect in the intensity profiles of selected atomic absorption lines. Theoretical spectra required for this analysis were calculated with the help of the MAGNESYN spectrum synthesis code described in Shulyak et al. (2017). Considering the large rotational Doppler broadening of the spectra of YY Gem A and B, it is impossible to derive unique field strength distributions composed of

multiple magnetic components as was done for slowly rotating M dwarfs in the latter study. Instead, we made use of a simpler two-component magnetic field model (e.g., Kochukhov & Lavail 2017) to represent the observed line profiles. This model assumes that a fraction of the surface f is covered by the field of strength B and the rest of the surface ($1-f$) is nonmagnetic. The total surface-averaged magnetic field strength is then given by $\langle B_I \rangle = B \cdot f$.

The thermodynamic structures of the magnetic and non-magnetic parts of the stellar surface were assumed to be the same and were approximated using models from the MARCS atmospheric grid. We assumed $T_{\text{eff}} = 3800$ K for both components as a compromise between the effective temperature 3820 ± 100 K given by Torres & Ribas (2002) and Stassun & Torres (2016) and $\approx 3770 \pm 100$ K determined by MacDonald & Mullan (2014). The surface gravity $\log g = 4.63$ was adopted according to the fundamental radius and mass of the mean component (Torres & Ribas 2002). The micro- and macroturbulent velocities are reported to be on the order of 100 m s^{-1} by the three-dimensional hydrodynamic simulations of M-dwarf atmospheres (Wende et al. 2009). Consequently, their exact choice has no impact on our analysis.

Large $v_e \sin i$ of the YY Gem components makes it impossible to study Zeeman splitting or broadening in spectral lines. Instead, we rely on the effect of magnetic intensification to measure surface magnetic fields. For instance, in the case of a saturated spectral line, its equivalent width is proportional to the magnetic field intensity and depends on the separation and number of individual Zeeman components, the so-called Zeeman splitting pattern (Landi Degl’Innocenti & Landolfi 2004). Therefore, at large $v_e \sin i$ values intensities of individual spectral lines in a magnetic star will depend on their Zeeman patterns and will vary from line to line, making it possible to deduce magnetic field strength even for the most rapidly rotating stars.

The key to a successful application of the Zeeman intensification methodology is finding a set of unblended spectral lines with accurately known relative strengths and a different magnetic field response. As demonstrated by Kochukhov & Lavail (2017) and Shulyak et al. (2017), a group of Ti I lines in the 964–979 nm wavelength interval satisfies these requirements for stars with spectral types from early M to about M6. There are nine mostly unblended Ti I features, with one of them (974.36 nm) having null effective Landé factor and thus being completely insensitive to a magnetic field. This line is useful for constraining nonmagnetic parameters, such as $v_e \sin i$ and Ti abundance. The remaining eight lines have effective Landé factors from 1.00 to 1.55 and different Zeeman splitting patterns (computed using the line data from the VALD3 database), resulting in a different magnetic field response. All these Ti I lines belong to the same multiplet formed by the fine-structure transitions between the a^3F and z^3F^o atomic terms. Their relative oscillator strengths are perfectly known, making it possible to accurately measure magnetic field strength by the spectrum synthesis fitting of the observed profiles of all or a subset of these Ti I lines.

Telluric absorption usually severely contaminates the wavelength interval in question. However, our spectral disentangling procedure described in Section 4 enabled an accurate telluric line removal and yielded clean, high-S/N average profiles of Ti lines suitable for precise magnetic field measurements.

The disentangled time-averaged spectra of YY Gem A and B derived above were corrected for the continuum dilution (e.g., Folsom et al. 2008) assuming equal luminosities of the components. The latter assumption appears to be adequate because, unlike the LSD profiles dominated by bluer lines, the disentangled spectra in the 963–985 nm region do not show a systematic line depth difference between the two components. The projected rotational velocity, Ti abundance, and magnetic field parameters were optimized with the Levenberg–Marquardt algorithm. We also allowed the code to vary continuum scaling factors for each spectral region (ensuring that fitting windows are sufficiently wide to include continuum on both sides of each line). This nonlinear least-squares fitting was applied to different combinations of Ti I lines to assess stability of the derived magnetic field parameters. This analysis showed that fits to two of the Ti I lines, 964.74 and 972.84 nm, yielded systematically higher residuals. The first of these features is located very close to the echelle order edge, is recorded at a lower S/N in all observations, and is shifted outside the wavelength coverage at some of the orbital phases. The second line has the smallest nonzero effective Landé factor for this Ti I multiplet and is blended by the Cr I 973.03 nm line. These two Ti I lines were therefore excluded from the fit. The final field strength and filling factor values were derived from simultaneous analysis of the seven remaining Ti I lines.

The titanium abundance recovered for the YY Gem components in different fitting attempts did not differ by more than 0.04 dex from the solar value of $\log(N_{\text{Ti}}/N_{\text{tot}}) = -7.09$ (Asplund et al. 2009). Considering that there are no physical reasons to expect a different chemical composition of the components of such a tight binary, we choose to adopt the solar Ti abundance for both components in the definitive analysis.

The final best-fitting model spectra are compared to observations in Figure 7. We also show the nonmagnetic synthetic spectra computed with the same Ti abundance and $v_e \sin i$. The effect of magnetic field is very prominent, especially for the Ti I 968.89, 977.03, 978.34, and 978.77 nm lines, which increase their equivalent width by up to 50% compared to the nonmagnetic spectrum. The resulting magnetic field parameters are given in Table 3. We obtained $\langle B_I \rangle = 3.44$ kG and $v_e \sin i = 37.7$ km s⁻¹ for YY Gem A and $\langle B_I \rangle = 3.15$ kG and $v_e \sin i = 37.9$ km s⁻¹ for YY Gem B. The filling factors were estimated to be in the 0.75–0.86 range. The projected rotational velocities determined here are consistent with $v_e \sin i$ that can be calculated from the rotational period, inclination angle, and the stellar radii determined in Section 5.1.

The formal statistical errors calculated by the least-squares optimization algorithm from the covariance matrix are often underestimating the true uncertainties. Rather than relying on these formal errors, we made a conservative uncertainty estimate by calculating the standard deviations of B , f , and the corresponding $\langle B_I \rangle$ values inferred from separate modeling of six magnetically sensitive Ti I lines with the titanium abundance and $v_e \sin i$ held constant. This analysis showed the line-to-line scatter of about 0.56 kG and 0.09 for the field strength and filling factor, respectively. On the other hand, their product remains the same to within 0.33 kG.

One may also be concerned that including a large number of magnetically sensitive lines biases the chi-square fit against the only magnetically insensitive feature, thereby leading to a degeneracy between magnetic field strength, $v_e \sin i$, and Ti

abundance. We tested this possibility by deriving the projected rotational velocity and titanium abundance from the nonmagnetic line alone and then fitting the magnetic field parameters using magnetically sensitive lines. This did not change any of the results reported above, suggesting that the primary reason for the dependence of magnetic parameters on line selection is not the intrinsic degeneracy of our spectral fitting procedure but, more likely, an unrecognized line blending, imperfect removal of telluric features, and, possibly, variation of the spectrograph’s instrumental profile across the echelle order.

According to the error analysis performed by Shulyak et al. (2017), variation of T_{eff} by 100 K leads to ≤ 0.05 kG change of $\langle B_I \rangle$ inferred for early M dwarfs. Thus, the Zeeman intensification results presented here are not significantly affected by ≈ 100 K uncertainty of the mean T_{eff} of the YY Gem components. Likewise, our neglect of the possible 90 K difference of the component temperatures (see Section 5.1) cannot lead to the 0.3 kG stronger mean field obtained for YY Gem A.

Finally, we have attempted to investigate rotational profile variability of individual Ti lines modeled in this section. Due to limited S/N of the observed data, we could not detect any profile variability pattern similar to the one seen in the LSD profiles constructed from bluer lines. We also did not detect any differential variability of the Ti I lines with large and small Landé factors. These results show that there are no significant nonuniformities in the surface distribution of the small-scale magnetic field in either of the YY Gem components and that these field strength inhomogeneities do not contribute to the Stokes I profile variation. This justifies approximating the entire stellar surface with a single magnetic field strength distribution.

7. Summary and Discussion

This study presented a comprehensive analysis of the surface magnetic fields of the components of the key benchmark early M eclipsing binary system YY Gem. We used high-quality archival spectropolarimetric observations to obtain precise radial velocity measurements and revise spectroscopic orbital elements, leading to an improved estimate of the component masses. The spectral disentangling technique was applied to separate contributions of the components in the mean intensity line profiles and in individual wavelength regions. We applied the tomographic imaging techniques of DI and ZDI to reconstruct maps of dark spots from variability of the mean intensity profiles and global magnetic field topologies from rotational modulation of the least-squares deconvolved circular polarization signatures. We then carried out a complementary analysis of the differential Zeeman intensification of individual magnetically sensitive atomic lines and inferred the total mean field strength at the surfaces of both YY Gem components.

7.1. The Global and Total Magnetic Fields of M Dwarfs

The outcome of our ZDI investigation indicates that both stars in the YY Gem system possess nonaxisymmetric, predominantly poloidal global magnetic field geometries. The dipolar components of these field structures are approximately anti-aligned, hinting at the magnetospheric interaction in the system. The mean global field strengths are found to be 205–260 G, with the primary exhibiting about 27% stronger field than the secondary. This difference in the global field

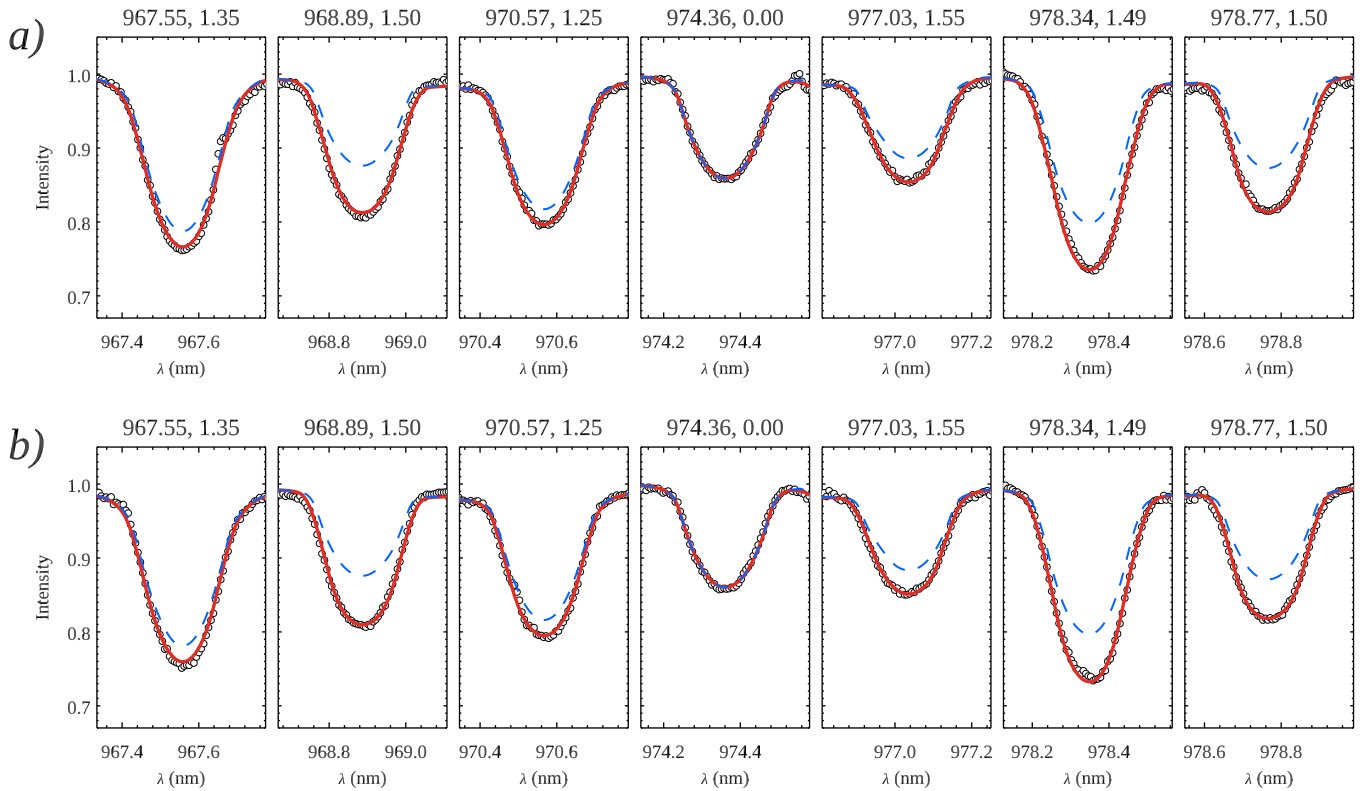


Figure 7. Zeeman broadening and intensification analysis for (a) YY Gem A and (b) YY Gem B using seven Ti I spectral lines in the 967.4–978.8 nm wavelength interval. The time-averaged, disentangled observed spectra (open circles) are compared with the best-fitting magnetic calculations (thick solid red line) and with the corresponding nonmagnetic spectrum synthesis (thin dashed blue line). The central wavelengths of the transitions and their effective Landé factors are indicated above each panel.

characteristics is consistent with the higher X-ray activity of the primary (Hussain et al. 2012). At the same time, the Zeeman intensification analysis yields the total mean field strengths of 3.44 and 3.15 kG for YY Gem A and B, respectively. The primary is still found to be more magnetized than the secondary, albeit only marginally so considering ~ 0.3 kG errors of these field strength measurements. This is reminiscent of the behavior of the components of the fully convective M-dwarf binary GJ 65 (Kochukhov & Lavail 2017), which also have nearly identical fundamental parameters and rotation periods and show comparable total field strengths while exhibiting vastly different global field geometries.

The much stronger field obtained with the Stokes I modeling indicates that the surface magnetic field topologies of YY Gem A and B are dominated by small-scale, tangled field structures, which are not detectable in Stokes V . Our study suggests that the ratio of the global to total field strength is 6.5%–7.6% or, equivalently, that only 0.4%–0.6% of the total magnetic field energy is contained in the global field. Reiners & Basri (2009) compared the global and total field strengths for six M dwarfs, showing that their ratio drops from $\sim 15\%$ in fully convective M dwarfs to only $\sim 0.5\%$ in early M stars. Our measurements for the components of YY Gem appear to agree with this trend.

The sample of M dwarfs with accurate Zeeman broadening field strength measurements has been significantly expanded since the work by Reiners & Basri (2009). It is therefore pertinent to reexamine the relation of global and total magnetic fields using new data. To this end, we combined information on the mean global field strengths $\langle B_V \rangle$ reported by ZDI studies of M dwarfs (Donati et al. 2008; Morin et al. 2008b, 2010;

Kochukhov & Lavail 2017) with the total field strengths $\langle B_I \rangle$ determined for the same stars from Stokes I analysis (Shulyak et al. 2017). Including results obtained here for the YY Gem components yields a sample of 22 individual M dwarfs with spectral types ranging from M0 to M6.5. Distribution of the field strength and field energy ratios as a function of stellar mass and total mean field strength is presented in Figure 8. The symbol size in this figure reflects the stellar rotation period, while the symbol style corresponds to the classification of global magnetic field topologies of M dwarfs into axisymmetric (mainly dipolar) and nonaxisymmetric (primarily multipolar) configurations according to Shulyak et al. (2017). In this framework, the components of YY Gem are grouped with multipolar stars, due to the large contribution of nondipolar and nonaxisymmetric harmonic modes.

The panels of Figure 8 suggest that a systematic trend of the fraction of magnetic energy contained in the global field component with stellar mass and total field strength is limited to a subgroup of stars with predominantly dipolar, axisymmetric global fields. Multipolar field stars do not show any obvious trends, although their position in the $\langle B_V \rangle / \langle B_I \rangle$ versus $\langle B_I \rangle$ plane agrees with the trend shown by M dwarfs with the global dipolar fields. The top panel of Figure 8 reveals that the two very active mid-M dwarfs Gl 65 B (UV Ceti) and Gl 51 have an unusually high global-to-total field strength ratio of $\sim 25\%$ (i.e., $\sim 6\%$ of the total field energy is stored in the global field component). One can therefore conclude that the fields in these stars have a weaker, though still dominant, local tangled contribution. Interestingly, Gl 412 B (WX UMa), which possesses the strongest known field in an M dwarf, deviates significantly from the general field complexity trends.

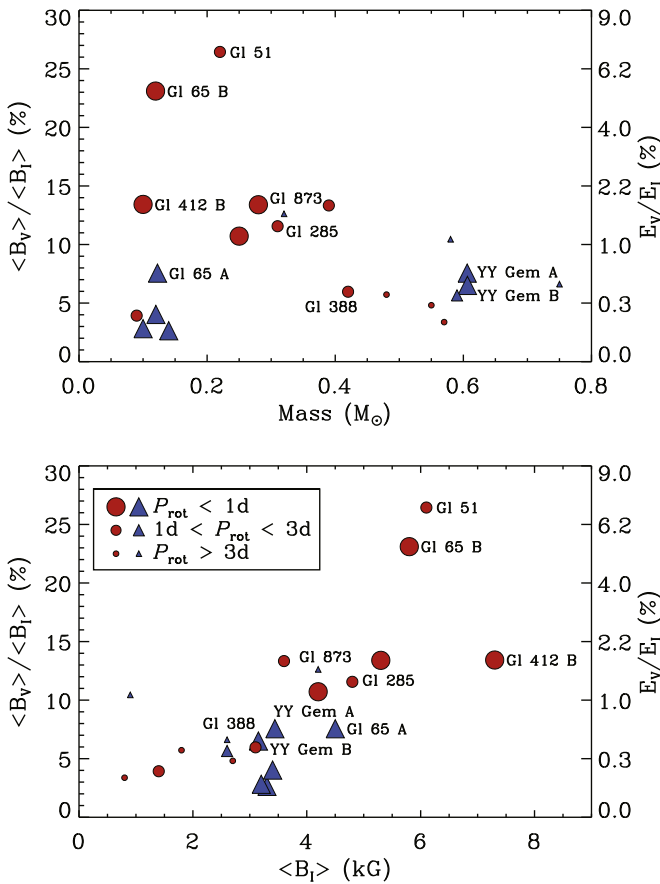


Figure 8. Ratio of the mean field strengths derived from Stokes V and Stokes I analyses and the corresponding magnetic field energy ratio as a function of stellar mass (top panel) and the field strength obtained from Stokes I (bottom panel). Red circles show stars with predominantly dipolar, axisymmetric fields. Blue triangles correspond to stars with nonaxisymmetric, multipolar fields. The symbol size reflects rotation period, as indicated by the legend in the bottom panel.

The main message of Figure 8 is that only a small fraction of the total magnetic field energy is visible in circular polarization and can thus be recovered by ZDI. This fraction varies from $<0.1\%$ to 7.0% , depending on the stellar parameters, the geometry of the global field, and the total field strength. This situation is very different from the behavior of massive, early-type stars with pure dipole-like fossil fields for which simple global magnetic field models are able to simultaneously reproduce both polarization and intensity magnetic observables (e.g., Landstreet & Mathys 2000; Kochukhov et al. 2015).

A complete characterization of an M-dwarf surface magnetic field therefore requires a combined investigation of the Zeeman effect in intensity spectra and polarization profile modeling with ZDI. The latter analysis alone cannot provide information about such key magnetic field characteristics as the total field strength. For this reason ZDI results should be used with extreme caution for inferences regarding underlying dynamo mechanism or its dependence on the stellar mass and rotation. How exactly the global (organized) and the local (tangled) magnetic field components combine at the stellar surface remains an open question. Some ideas of what such composite field geometries may look like have been proposed based on empirical arguments (Lang et al. 2014) and ab initio three-dimensional MHD simulations (Yadav et al. 2015). However, since no comprehensive polarized spectrum synthesis

calculations were carried out for either of these modeling frameworks, it is not known how they would fare when confronted with real observations.

7.2. Testing Predictions of Magnetoconvection Stellar Structure Models of Low-mass Stars

Detailed characterization of the surface magnetic field of the components of YY Gem provided by our study puts us in the position to directly test predictions of the magnetic stellar interior structure models developed for this system with the aim to explain the inflated radii. In one of such studies Feiden & Chaboyer (2013) were able to reproduce the observed mean radius of the YY Gem components by invoking stabilization of the interior convection by a magnetic field. They found that the surface magnetic field strength required by their best-fitting models lies in the range from 4.0 to 4.5 kG, which is only 20% – 40% higher than the total surface field strength $\langle B_I \rangle$ measured here using Zeeman intensification.

An alternative approach to incorporating effects of a magnetic field in one-dimensional interior models of low-mass stars was developed by Mullan & MacDonald (2001) and MacDonald & Mullan (2014). The latter paper presented an in-depth modeling of the YY Gem system and showed that its properties can be reproduced with various interior magnetic field profiles corresponding to a 240 – 420 G vertical field on the stellar surface. MacDonald & Mullan (2017b) have subsequently revised this prediction to 490 – 550 G.

There is some confusion in the literature regarding the specific magnetic field observable that should be compared with the mean vertical field discussed in these theoretical papers. MacDonald & Mullan (2017a) argued that their vertical surface field parameter corresponds to the global field inferred by ZDI while the surface field in Feiden & Chaboyer (2013) models should be compared to $\langle B_I \rangle$ measurements. On the other hand, in their recent study of the wide M-dwarf binary GJ 65 MacDonald et al. (2018) compared their model predictions with $\langle B_I \rangle$ rather than with any field characteristics obtained from circular polarization modeling.

Considering our ZDI results, the mean vertical field corresponds to the surface-averaged unsigned radial field $\langle |B_r| \rangle$ reported in Table 3. Our $\langle |B_r| \rangle = 98$ – 168 G is a factor of 2.9 – 5.6 lower than the vertical surface fields suggested by MacDonald & Mullan (2017b). If, instead, we choose to compare their predictions with our $\langle B_I \rangle$ measurements, the theoretically estimated field should be multiplied by $\sqrt{3}$ assuming isotropic field vector orientation. This yields a total surface field strength of 850 – 950 G, which is 3.3 – 4.0 times lower than $\langle B_I \rangle$ determined in our paper.

To summarize, theoretical models by Feiden & Chaboyer (2013) appear to predict a more realistic surface field strength for the components of YY Gem than the one found in the approach by MacDonald & Mullan (2014, 2017b). However, this conclusion should be taken with caution given the ambiguity of relating the vertical surface field parameter of the latter theoretical calculations to observations.

7.3. Estimating Magnetic Flux from X-Ray Luminosity

In the absence of direct constraints on the surface magnetic properties, many studies resort to an approximate estimate of the mean magnetic field strength. The X-ray emission is often considered to be a particularly useful magnetic proxy.

Pevtsov et al. (2003) demonstrated that the total unsigned magnetic flux measured for solar magnetic regions at different spatial scales shows a power-law dependence on the X-ray spectral radiance. The few $\langle B_l \rangle$ measurements reported at that time for active late-type stars fell on the extrapolation of this relation to higher magnetic flux values. Feiden & Chaboyer (2013) recalibrated this relation using Stokes I field strength measurements of low-mass dwarfs. Both Feiden & Chaboyer (2013) and MacDonald & Mullan (2014) attempted to verify their theoretically predicted surface field strengths with indirect field strength estimates using the X-ray emission of YY Gem. This exercise was, however, hampered by the contamination of the *ROSAT* X-ray measurements of YY Gem (Voges et al. 1999) by the nearby early-type companions Castor A and B.

More recent *Chandra* observations of YY Gem (Hussain et al. 2012) provided images with a high angular resolution, allowing one to separate the low-mass binary from the A-type stars. The combined quiescent X-ray luminosity of YY Gem is reported to be $(3\text{--}3.5) \times 10^{29} \text{ erg s}^{-1}$. Assuming equal luminosities of the components and using their fundamental radii yields $\langle B_l \rangle = 770\text{--}820 \text{ G}$ with the calibration by Feiden & Chaboyer (2013). This is significantly smaller than the observed $\langle B_l \rangle$ obtained in our study, indicating that the magnetic flux versus X-ray luminosity relation may be appropriate only for large stellar samples but is unlikely to be precise enough to provide a meaningful field strength estimate for individual stars.

Another problematic issue with applying this relation to active stars, apparently entirely overlooked in the literature, is that for the Sun the total magnetic flux is defined as a surface integral of the unsigned vertical field component $|B_z|$ (Fisher et al. 1998). Therefore, an extension of this relation to stars requires introducing a correction factor, dependent on the surface field geometry (e.g., $\sqrt{3}$ for isotropic field, 1.38 for a dipolar field topology, a value $\gg 1$ for a field configuration dominated by the toroidal component), to account for the difference between $\langle |B_z| \rangle$ and $\langle B_l \rangle$. This correction would systematically reduce the observed surface magnetic fluxes for stars employed to calibrate the relation with X-ray luminosity. Since the ratio of poloidal and toroidal magnetic energy is known to change systematically with stellar parameters and mean magnetic field strength (Petit et al. 2008; See et al. 2015), it is plausible to expect that this reduction is not universal but varies significantly from one star to another.

7.4. Spot Filling Factor for the Components of YY Gem

The tomographic mapping of starspots carried out here for YY Gem provided new detailed information on the characteristics of nonuniform brightness distributions on these stars. We found that both components possess low-contrast, relatively small-scale surface features, concentrated at low latitudes. If we interpret our Doppler imaging maps in terms of the fractional coverage by completely dark spots, we infer a spot coverage of $< 1\%$ for both components. This can be compared with 3% spot coverage obtained with the help of photometric light-curve modeling assuming few large circular spots located at fixed latitudes (Torres & Ribas 2002).

Formation of cool spots on the surfaces of magnetically active late-type stars was proposed as an alternative explanation of their increased radii (Chabrier et al. 2007). MacDonald & Mullan (2014) applied this hypothesis to YY Gem, finding that dark spots must cover more than 40% of the surface area of

each component in order to match the observed radii. Likewise, Jackson & Jeffries (2014) estimated that the observed radius inflation of young stars in open clusters and low-mass eclipsing binaries, including YY Gem, can be reproduced by stellar models with starspot filling factors in the 35%–51% range. This assessment corresponds to completely dark spots. The required spot coverage must be even larger for a finite spot-to-photosphere brightness contrast. Such extreme surface inhomogeneities are clearly not observed for YY Gem. Our detailed line profile analysis also shows no evidence of polar spots that could have been missed by previous photometric studies. In general, cool polar caps appear to be uncommon on rapidly rotating early to mid-M dwarfs (Barnes et al. 2004, 2017; Morin et al. 2008a). Therefore, we conclude that our results do not support any theoretical explanation of the properties of YY Gem that involves postulating substantial cool spot coverage. On the other hand, we cannot exclude existence of numerous, homogeneously distributed small spots with sizes below the resolution limit ($\approx 10^\circ$) of our DI analysis. This scenario can be tested with very high precision photometric monitoring of eclipses in the YY Gem system. The required observational data may be provided by the *TESS* mission (Ricker et al. 2016), which is scheduled to observe YY Gem in 2020 January.

O.K. acknowledges support by the Knut and Alice Wallenberg Foundation (project grant “The New Milky Way”), the Swedish Research Council (project 621-2014-5720), and the Swedish National Space Board (projects 185/14, 137/17). D.S. acknowledges support by DFG in the framework of the project “CRC 963: Astrophysical Flow Instabilities and Turbulence” (projects A16 and A17). The authors thank Ansgar Reiners for fruitful discussions.

This paper is based on observations obtained at the CFHT, which is operated by the National Research Council of Canada, the Institut National des Sciences de l’Univers (INSU) of the Centre National de la Recherche Scientifique (CNRS) of France, and the University of Hawaii. Archival data were retrieved using facilities of the Canadian Astronomy Data Centre operated by the National Research Council of Canada with the support of the Canadian Space Agency.

This work has made use of the VALD database, operated at Uppsala University, the Institute of Astronomy RAS in Moscow, and the University of Vienna.

Facility: CFHT (ESPaDOs spectropolarimeter).

ORCID iDs

Oleg Kochukhov  <https://orcid.org/0000-0003-3061-4591>
 Denis Shulyak  <https://orcid.org/0000-0001-8496-2482>

References

- Asplund, M., Grevesse, N., Sauval, A. J., & Scott, P. 2009, *ARA&A*, 47, 481
 Bagnulo, S., Landolfi, M., Landstreet, J. D., et al. 2009, *PASP*, 121, 993
 Barnes, J. R., James, D. J., & Collier Cameron, A. 2004, *MNRAS*, 352, 589
 Barnes, J. R., Jeffers, S. V., Haswell, C. A., et al. 2017, *MNRAS*, 471, 811
 Basri, G., Marcy, G. W., & Valenti, J. A. 1992, *ApJ*, 390, 622
 Butler, C. J., Erkan, N., Budding, E., et al. 2015, *MNRAS*, 446, 4205
 Chabrier, G., Gallardo, J., & Baraffe, I. 2007, *A&A*, 472, L17
 Claret, A. 2017, *A&A*, 600, A30
 Cotton, D. V., Bailey, J., & Kedziora-Chudczar, L. 2014, *MNRAS*, 439, 387
 Donati, J.-F., Morin, J., Petit, P., et al. 2008, *MNRAS*, 390, 545
 Donati, J.-F., Semel, M., Carter, B. D., Rees, D. E., & Collier Cameron, A. 1997, *MNRAS*, 291, 658

- Eker, Z., Soydugan, F., Soydugan, E., et al. 2015, *AJ*, **149**, 131
- Feiden, G. A., & Chaboyer, B. 2012, *ApJ*, **761**, 30
- Feiden, G. A., & Chaboyer, B. 2013, *ApJ*, **779**, 183
- Feiden, G. A., & Chaboyer, B. 2014, *ApJ*, **789**, 53
- Fisher, G. H., Longcope, D. W., Metcalf, T. R., & Pevtsov, A. A. 1998, *ApJ*, **508**, 885
- Folsom, C. P., Kochukhov, O., Wade, G. A., Silvester, J., & Bagnulo, S. 2010, *MNRAS*, **407**, 2383
- Folsom, C. P., Wade, G. A., Kochukhov, O., et al. 2008, *MNRAS*, **391**, 901
- Gao, D. H., Chen, P. F., Ding, M. D., & Li, X. D. 2008, *MNRAS*, **384**, 1355
- Güdel, M., Audard, M., Magee, H., et al. 2001, *A&A*, **365**, L344
- Gustafsson, B., Edvardsson, B., Eriksson, K., et al. 2008, *A&A*, **486**, 951
- Hackman, T., Lehtinen, J., Rosén, L., Kochukhov, O., & Käpylä, M. J. 2016, *A&A*, **587**, A28
- Hatzes, A. P. 1995, in IAU Symp. 176, Stellar Surface Structure, ed. Klaus G. Strassmeier (Vienna: Kluwer), 90
- Hussain, G. A. J., Brickhouse, N. S., Dupree, A. K., et al. 2012, *MNRAS*, **423**, 493
- Jackson, R. J., & Jeffries, R. D. 2014, *MNRAS*, **445**, 4306
- Kochukhov, O. 2007, in Physics of Magnetic Stars, ed. I. I. Romanyuk & D. O. Kudryavtsev (Nizhniy Arkhyz, Special Astrophysical Observatory of RAS), 109
- Kochukhov, O. 2016, *LNP*, **914**, 177
- Kochukhov, O. 2017, *A&A*, **597**, A58
- Kochukhov, O., Johnston, C., Alecian, E., & Wade, G. A. 2018, *MNRAS*, **478**, 1749
- Kochukhov, O., & Lavail, A. 2017, *ApJL*, **835**, L4
- Kochukhov, O., Lüftinger, T., Neiner, C., Alecian, E. & MiMeS Collaboration 2014, *A&A*, **565**, A83
- Kochukhov, O., Makaganiuk, V., & Piskunov, N. 2010, *A&A*, **524**, A5
- Kochukhov, O., Rusomarov, N., Valenti, J. A., et al. 2015, *A&A*, **574**, A79
- Kron, G. E. 1952, *ApJ*, **115**, 301
- Landi Degl'Innocenti, E., & Landolfi, M. 2004, Polarization in Spectral Lines, Astrophysics and Space Science Library Vol. 307 (Dordrecht: Kluwer)
- Landstreet, J. D., & Mathys, G. 2000, *A&A*, **359**, 213
- Lang, P., Jardine, M., Morin, J., et al. 2014, *MNRAS*, **439**, 2122
- López-Morales, M. 2007, *ApJ*, **660**, 732
- MacDonald, J., & Mullan, D. J. 2013, *ApJ*, **765**, 126
- MacDonald, J., & Mullan, D. J. 2014, *ApJ*, **787**, 70
- MacDonald, J., & Mullan, D. J. 2017a, *ApJ*, **834**, 67
- MacDonald, J., & Mullan, D. J. 2017b, *ApJ*, **850**, 58
- MacDonald, J., Mullan, D. J., & Dieterich, S. 2018, *ApJ*, **860**, 15
- Markwardt, C. B. 2009, in ASP Conf. Ser. 411, Astronomical Society of the Pacific Conference Series, ed. D. A. Bohlender, D. Durand, & P. Dowler (San Francisco, CA: ASP), 251
- Marsden, S. C., Petit, P., Jeffers, S. V., et al. 2014, *MNRAS*, **444**, 3517
- Morales, J. C., Gallardo, J., Ribas, I., et al. 2010, *ApJ*, **718**, 502
- Morales, J. C., Ribas, I., & Jordi, C. 2008, *A&A*, **478**, 507
- Morales, J. C., Ribas, I., Jordi, C., et al. 2009a, *ApJ*, **691**, 1400
- Morales, J. C., Torres, G., Marschall, L. A., & Brehm, W. 2009b, *ApJ*, **707**, 671
- Morin, J., Donati, J.-F., Forveille, T., et al. 2008a, *MNRAS*, **384**, 77
- Morin, J., Donati, J.-F., Petit, P., et al. 2008b, *MNRAS*, **390**, 567
- Morin, J., Donati, J.-F., Petit, P., et al. 2010, *MNRAS*, **407**, 2269
- Moya, A., Zuccarino, F., Chaplin, W. J., & Davies, G. R. 2018, *ApJS*, **237**, 21
- Mullan, D. J., & MacDonald, J. 2001, *ApJ*, **559**, 353
- Petit, P., Dintrans, B., Solanki, S. K., et al. 2008, *MNRAS*, **388**, 80
- Pevtsov, A. A., Fisher, G. H., Acton, L. W., et al. 2003, *ApJ*, **598**, 1387
- Reiners, A. 2012, *LRSP*, **9**, 1
- Reiners, A., & Basri, G. 2009, *A&A*, **496**, 787
- Ribas, I. 2006, *Ap&SS*, **304**, 89
- Ricker, G. R., Vanderspek, R., Winn, J., et al. 2016, *Proc. SPIE*, **9904**, 99042B
- Rosén, L., Kochukhov, O., Alecian, E., et al. 2018, *A&A*, **613**, A60
- Ryabchikova, T., Piskunov, N., Kurucz, R. L., et al. 2015, *PhyS*, **90**, 054005
- See, V., Jardine, M., Vidotto, A. A., et al. 2015, *MNRAS*, **453**, 4301
- Shulyak, D., Reiners, A., Engeln, A., et al. 2017, *NatAs*, **1**, 0184
- Stassun, K. G., & Torres, G. 2016, *AJ*, **152**, 180
- Stelzer, B., Burwitz, V., Audard, M., et al. 2002, *A&A*, **392**, 585
- Torres, G. 2013, *AN*, **334**, 4
- Torres, G., Andersen, J., & Giménez, A. 2010, *A&ARv*, **18**, 67
- Torres, G., & Ribas, I. 2002, *ApJ*, **567**, 1140
- Vidotto, A. A., Gregory, S. G., Jardine, M., et al. 2014, *MNRAS*, **441**, 2361
- Voges, W., Aschenbach, B., Boller, T., et al. 1999, *A&A*, **349**, 389
- Wende, S., Reiners, A., & Ludwig, H.-G. 2009, *A&A*, **508**, 1429
- Yadav, R. K., Christensen, U. R., Morin, J., et al. 2015, *ApJL*, **813**, L31